A study of the fine-scale motions of incompressible time-developing mixing layers

Cite as: Physics of Fluids **6**, 871 (1994); https://doi.org/10.1063/1.868323
Submitted: 17 May 1993 . Accepted: 27 August 1993 . Published Online: 04 June 1998

J. Soria, R. Sondergaard, B. J. Cantwell, M. S. Chong, and A. E. Perry

A study of the fine-scale motions of incompressible time-developing mixing layers

J. Soria
C.S.I.R.O., Highett, Australia

R. Sondergaard and B. J. Cantwell
Department of Aeronautics and Astronautics, Stanford University, Stanford, California 94305

M. S. Chong and A. E. Perry
Department of Mechanical Engineering, University of Melbourne, Melbourne, Australia

(Received 17 May 1993; accepted 27 August 1993)

The geometry of dissipating motions in direct numerical simulations (DNS) of the incompressible mixing layer is examined. All nine partial derivatives of the velocity field are determined at every grid point in the flow, and various invariants and related quantities are computed from the velocity gradient tensor. Motions characterized by high rates of kinetic energy dissipation and high enstrophy density are of particular interest. Scatter plots of the invariants are mapped out and interesting and unexpected patterns are seen. Depending on initial conditions, each type of shear layer produces its own characteristic scatter plot. In order to provide more detailed information on the distribution of invariants at intermediate and large scales, scatter plots are replaced with more useful number density contour plots. These essentially represent the unnormalized joint probability density function of the two invariants being cross-plotted. Plane mixing layers at the same Reynolds number, but with laminar and turbulent initial conditions, are studied, and comparisons of the rate-of-strain topology of the dissipating motions are made. The results show conclusively that, regardless of initial conditions, the bulk of the total kinetic energy dissipation is contributed by intermediate scale motions, whose local rate-of-strain topology is characterized as unstable-node-saddle–saddle (two positive rate-of-strain eigenvalues, one negative). In addition, it is found that, for these motions, the rate-of-strain invariants tend to approximately follow a straight line relationship, characteristic of a two-dimensional flow with out of plane straining. In contrast, fine-scale motions, which have the highest dissipation, but which only contribute a small fraction of the total dissipation tend toward a fixed ratio of the principal rates of strain.

I. BACKGROUND AND METHOD OF APPROACH

Direct numerical simulations of turbulence generate vast amounts of information, and efficient methods are needed for identifying significant features in the data. In the present approach, a concise description of the flow is produced in terms of cross-plots of the invariants of the velocity gradient tensor. These plots reveal significant features of the data, which would be difficult or impossible to find using standard visual display techniques. Reference 1 is essentially a road map for relating tensor invariants to local flow patterns in compressible and incompressible flows. Figure 1 shows the various possibilities that can occur in an incompressible flow. It should be noted that the method can be applied to the gradient tensor of any smooth vector field that may be of interest, including the vorticity field, pressure gradient field, and concentration gradient field.

There are several reasons for studying velocity gradient tensor invariants. First, because one is working with the invariants, the results obtained are coordinate independent (invariant under an affine transformation). Moreover, the velocity gradients are independent of the frame of reference of a moving observer. Second, in the case of incompressible flow for which the first invariant is zero, an infinite three-dimensional field can be collapsed into a compact region of a two-dimensional space. Finally, turbulent flow is characterized by a wide range of scales. Relatively small velocity gradients on the order of U/δ occur at large scales, and much larger gradients on the order of $U/\delta(R_\delta)^{1/2}$ occur at small scales. The quantities U and δ are integral velocity and length scales and R_δ is the flow Reynolds number. The sorting of different length scales into different regions of the invariant plots permits general topological features of various scales to be easily identified.

An important aspect of the method is the association which can be made between structural features of the invariant plots and local flow patterns in physical space. This has turned out to be a very sensitive way to pick up subtle but possibly important properties of the flow field in physical space. For example, the method was recently used to identify local vortex breakdown in streamwise vortices in a plane mixing layer. Invariant plots studied by Chen *et al.*[2] revealed a region within the streamwise vortices, where the topology alternately changes from stable-focus stretching to unstable-focus compressing. Subsequent detailed studies in physical space by Lopez and Bulbeck[3] revealed that these regions contain all the kinematic features characteristic of spiral vortex breakdown.

 1070-6631/94/6(2)/871/14/$6.00

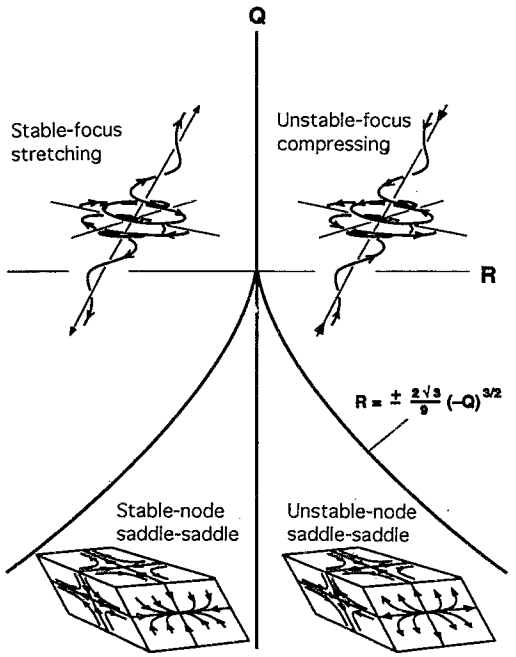

FIG. 1. Three-dimensional topologies in the Q-R(P=0) plane.

II. THE VELOCITY GRADIENT TENSOR

The velocity gradient tensor may be broken up into a symmetric and an antisymmetric part, $A_{ij}=\partial u_i/\partial x_j = S_{ij}+W_{ij}$, where $S_{ij}=(\partial u_i/\partial x_j+\partial u_j/\partial x_i)/2$ and $W_{ij}=(\partial u_i/\partial x_j-\partial u_j/\partial x_i)/2$ are the rate-of-strain and rate-of-rotation tensors, respectively. The eigenvalues of A_{ij} satisfy the characteristic equation

$$\lambda^3+P\lambda^2+Q\lambda+R=0, \tag{1}$$

where the matrix invariants are

$$P=-(A_{11}+A_{22}+A_{33})=-\text{trace}[A]=-S_{ii}, \tag{2}$$

$$Q=\begin{vmatrix}A_{11} & A_{12}\\ A_{21} & A_{22}\end{vmatrix}+\begin{vmatrix}A_{11} & A_{13}\\ A_{31} & A_{33}\end{vmatrix}+\begin{vmatrix}A_{22} & A_{23}\\ A_{32} & A_{33}\end{vmatrix}$$

$$=\tfrac{1}{2}(P^2-\text{trace}[A^2])=\tfrac{1}{2}(P^2-S_{ij}S_{ji}-W_{ij}W_{ji}]), \tag{3}$$

and

$$R=-\begin{vmatrix}A_{11} & A_{12} & A_{13}\\ A_{21} & A_{22} & A_{23}\\ A_{31} & A_{32} & A_{33}\end{vmatrix}$$

$$=-\det[A]$$

$$=\tfrac{1}{3}(-P^3+3PQ-\text{trace}[A^3])$$

$$=\tfrac{1}{3}(-P^3+3PQ-S_{ij}S_{jk}S_{ki}-3W_{ij}W_{jk}S_{ki}). \tag{4}$$

It can be shown that, in the P–Q–R space of matrix invariants, the surface that divides characteristic equations with three real eigenvalues from characteristic equations with one real and two complex eigenvalues is

$$27R^2+(4P^3-18PQ)R+(4Q^3-P^2Q^2)=0. \tag{5}$$

A detailed discussion of the properties of this surface is given in Chong, Perry, and Cantwell,[1] along with a guide to the various possible elementary flow patterns that can occur in different domains.

Much of the discussion in this paper concerns the symmetric part of the velocity gradient tensor, the second invariant of which is proportional to the negative of the kinetic energy dissipation. The invariants of the rate-of-strain tensor, P_S, Q_S, and R_S are generated by setting the components of W_{ij} to zero in the above relations. The flows considered are, with one exception, incompressible; hence $P=P_S=0$. Thus the local geometry of the flow is completely described by the second and third invariants (Q,R) and (Q_S,R_S). The second invariant of the rate-of-rotation tensor, Q_W, obtained by setting P and S_{ij} to zero, is nonzero and is proportional to the enstrophy density $(\omega_i\omega_i/2)$. The first and third invariants of W_{ij} are identically zero.

Figure 1 illustrates the various flow topologies that can occur in the plane $P=0$. The intersection of this plane with the surface (5) is given by

$$R=\pm\frac{2\sqrt{3}}{9}(-Q)^{3/2}, \tag{6}$$

which divides real solutions from complex solutions, as indicated. For the case $P=0$, the second invariant is

$$Q=\tfrac{1}{2}(W_{ij}W_{ij}-S_{ij}S_{ij}), \tag{7}$$

where the indices have been switched to indicate explicitly that Q is formed from the difference of two terms, each of which is a positive sum of squares. The local topology has complex or real eigenvalues depending on whether the (Q,R) pair evaluated at a given point in the flow lies above or below (6).

The mechanical dissipation of kinetic energy due to viscous friction is

$$\phi=2\nu S_{ij}S_{ij}=-4\nu Q_S. \tag{8}$$

Large negative values of Q_S correspond to large rates of dissipation of kinetic energy. Large negative values of Q indicate regions where the strain is both large and strongly dominant over the enstrophy. Large positive values of Q indicate the reverse.

III. CONSTRUCTION OF INVARIANT PLOTS

The invariant plot method for analyzing flow fields was first developed by Chen *et al.*,[2] and the procedure for constructing the plots is summarized as follows: (i) The nine partial derivatives of the velocity gradient tensor are evaluated at every point in the computed field; (ii) the invariants Q, R, Q_S, R_S, and Q_W are determined at every point; and (iii) the resulting (Q,R), (Q_S,R_S), and $(-Q_S,Q_W)$ pairs are cross-plotted, resulting in scatter diagrams typified by the results shown in Fig. 2.

In practice, while the scatter plots are very useful for revealing topological features of the finest-scale motions which are characterized by the largest gradients in the flow, lower gradient motions characterizing intermediate or larger scales are obscured by layers and layers of over-

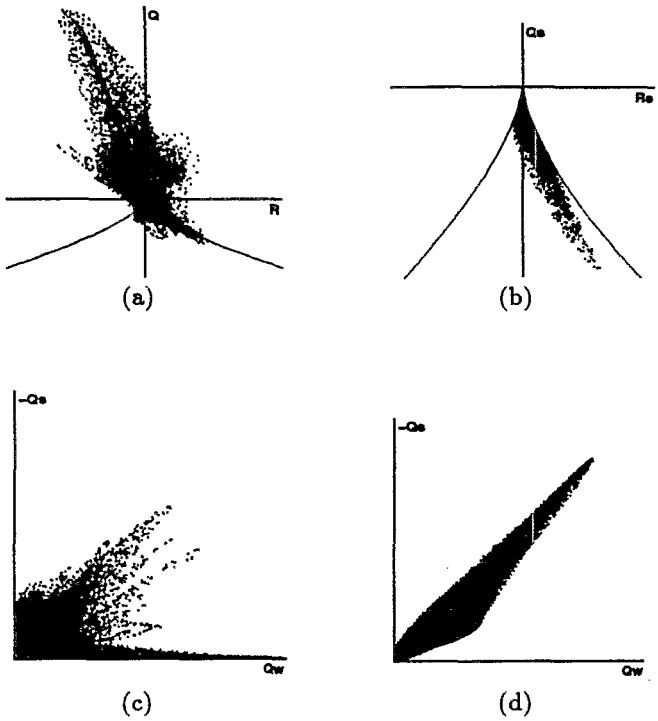

FIG. 2. Scatter plots of (a) Q vs R; (b) Q_S vs R_S; (c) $-Q_S$ vs Q_W for *HIGH1P* at $tU/\delta_0=29.8$; and (d) Q_S vs Q_W for a compressible mixing layer computed by Chen[6] at $tU/\delta_0=72.0$.

lapping points. To remedy this the scatter plots are replaced by plots of contours of the number density of points (corrected for nonuniform grid spacing) lying within a unit area in invariant space. These plots are essentially equivalent to unnormalized plots of the joint probability density function. Because of the extreme variations of number density that occur, contour levels are chosen logarithmically to have the values 1, 10, 100, 1000, etc. Choosing the lowest contour value to be unity ensures that isolated points are captured thus retaining the features of the scatter plot far from the origin, while providing information about the distribution of invariants near the origin corresponding to intermediate- and large-scale motions. This is the basis of Figs. 6–18 and 22–24.

IV. DISCUSSION OF RESULTS

A. Simulation cases studied

We consider in this paper several cases of the incompressible ($P=0$) plane mixing layer computed by Moser and Rogers.[4,5] Three direct numerical simulations are considered, namely, *HIGH1P*, *HIGH2P*, and *tbl*. The cases *HIGH1P* and *HIGH2P* were initiated from laminar error function profiles to which were added small disturbances in the form of streamwise vortices. The case *tbl* was initiated with two turbulent boundary layer realizations with equal and opposite free-stream velocities placed on opposite sides of a dividing plate, which was dissolved at time $t=0$. The initial turbulent boundary layers were DNS computations of Spalart.[6] All cases were computed as time developing layers, and Table I shows the initial Reynolds numbers of

TABLE I. Flow parameters.

	HIGH1P	*HIGH2P*	*tbl*
U_2-U_1	2	2	2
Initial vorticity thickness, δ_0	1	1	1.4
Viscosity, ν	$\frac{1}{250}$	$\frac{1}{250}$	$\frac{1}{500}$
Initial Re$=(U_2-U_1)\delta_0/2\nu$	250	250	700

the three cases of interest. Details of the *HIGH1P* and *HIGH2P* results have been reported by Moser and Rogers.[5] See Table II of Ref. 5 for a detailed description of initial conditions. Unless otherwise stated, all results in the present paper are normalized by half the velocity difference across the layer, U, and the initial vorticity thickness δ_0.

B. Scatter plots

Figures 2(a)–2(c) show scatter diagrams for *HIGH1P* taken from Chen *et al.*[2] These diagrams are made up of the entire data set for a given time step. Figure 2(a) shows that the bulk of the data tends to be concentrated near the origin, while most of the high gradient motions lie either in the lower right quadrant or along a nearly straight ridge line in the upper left quadrant with the local topology stable-focus stretching. When only the symmetric part of the velocity gradient field is studied, as in Fig. 2(b), it is seen that there is a strong tendency to the rate-of-strain topology unstable-node-saddle–saddle. Figure 2(c) is particularly interesting. Figure 3 schematically indicates the physical interpretation for various regions of Fig. 2(c). Data that falls on a 45° line through the origin represents points in the flow with high dissipation accompanied by high enstrophy density. It can be shown that such points are consistent with the physical picture of a local vortex sheet, where most of the rate of strain is dominated by the velocity gradient within the sheet. Data that lies along the horizontal axis represents points with high enstrophy but little dissipation, as would occur in solid body rotation near the center of a vortex tube. Note that there is a tendency for points with the largest enstrophy to be of this type. In the work of Chen *et al.*[2] this data was traced to

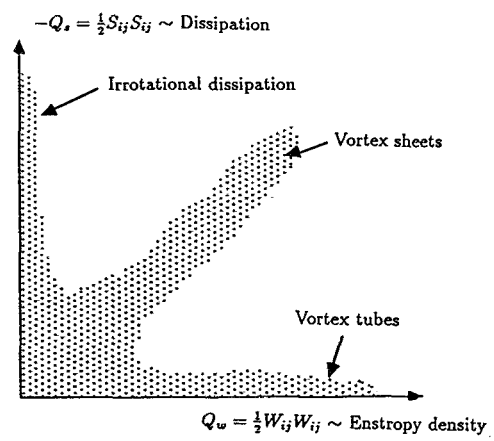

FIG. 3. Physical interpretation of various regions in the $-Q_S$ vs Q_W plot.

regions of high enstrophy lying within streamwise rib vortices, which connect adjacent spanwise rollers in the *HIGH1P* simulation. Data along the vertical axis represents points where the enstrophy density is considerably smaller than the dissipation. In the simulations studied here such points, although they are fairly common, tend not to be associated with very large rates of dissipation [cf. Fig. 2(b)]. As a matter of interest, Fig. 2(d) shows a plot from a compressible plane mixing layer computation by Chen.[6] This flow is slightly compressible, and the indication is that in this case virtually all the motion is in the form of vortex sheets (high enstrophy corresponding to high dissipation).

C. Mean dissipation

Classical arguments, based on the idea that dissipation of turbulent kinetic energy scales with production, lead to the following estimates:

$$\epsilon = 2\nu\overline{S'_{ij}S'_{ij}} \cong -\overline{u'v'}\frac{\partial \bar{U}}{\partial y}, \tag{9}$$

where the S'_{ij} are fluctuating, non-normalized strain rates. Results from experiment show that for fully developed shear layers,

$$-\frac{\overline{u'v'}}{(2U)^2} \cong 0.012. \tag{10}$$

From (9) and (10) and using $\partial\bar{U}/\partial y \cong 2U/\delta$, we have

$$\epsilon = 2\nu\overline{S'_{ij}S'_{ij}} = 0.096\frac{U^3}{\delta}. \tag{11}$$

For time $tU/\delta_0 = 29.8$ in *HIGH1P*, where the vorticity thickness has increased by a factor of 6.5 over the initial thickness, the Reynolds number R_δ based on the current vorticity thickness, δ, and the velocity difference across the layer, $2U$, is 3000. Hence

$$-Q_S = \frac{\overline{S'_{ij}S'_{ij}}\delta_0^2}{2U^2} \cong \frac{0.096}{8} R_\delta \left(\frac{\delta_0}{\delta}\right)^2 = 0.852. \tag{12}$$

One would expect the average value of $-Q_S$ at the midplane of the mixing layer to be of this order. Profiles of $-Q_S$ averaged over horizontal planes in the mixing layer at various times are shown in Fig. 4(a). The average at the midplane agrees quite well with the estimate indicated by (12), which is indicative of the production of kinetic energy. This result is consistent with the fully developed time-averaged value obtained from experiments by Bradshaw and Ferriss.[7] An order of magnitude analysis similar to (12) reported by Chen *et al.*,[2] giving the value of 18.2, was in error due to incorrect normalization of the variables.

Figures 4(b) and 4(c) show the horizontally averaged $-Q_S$ for *HIGH2P* and *tbl*. Along with providing information on the mean dissipation, these figures also indicate the growth of each layer at successive times. A feature to note here, which will be returned to in the later discussion, is the considerably more rapid growth of *HIGH2P* compared to *tbl*. Another feature of Figs. 4(a)–4(c) concerns the

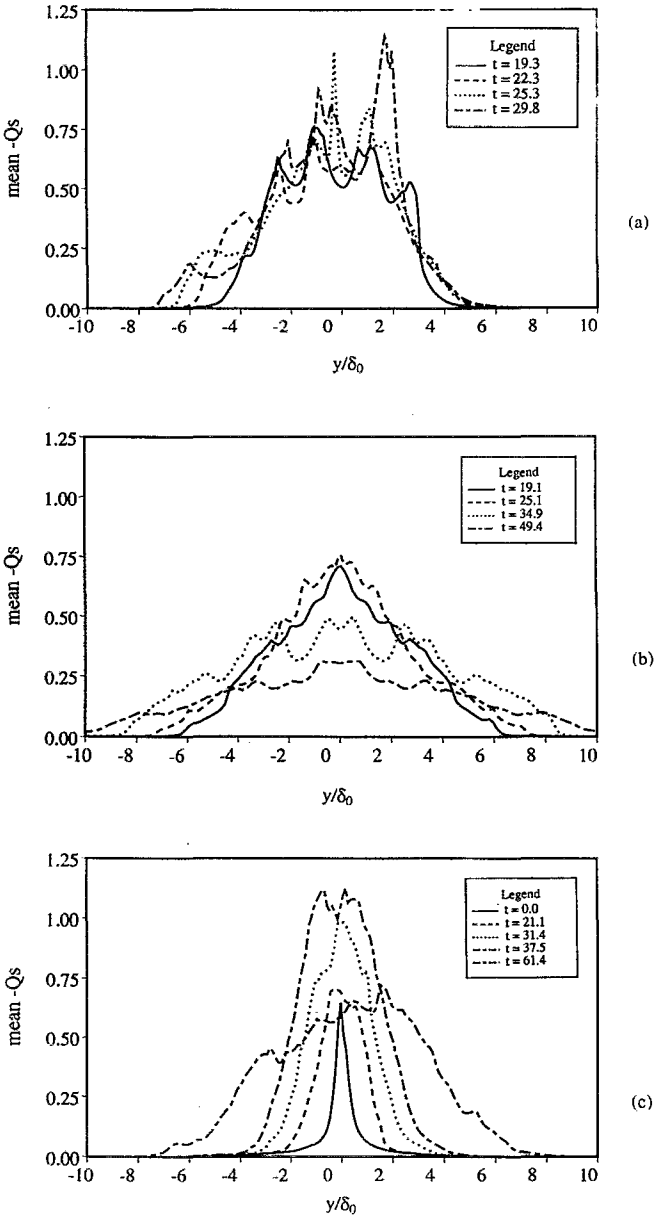

FIG. 4. Planar x-z average Q_S versus cross-stream direction y/δ_0 for (a) *HIGH1P* at $tU/\delta_0 = 19.3$, 22.3, 25.3, and 29.8; (b) *HIGH2P* at $tU/\delta_0 = 19.1$, 25.1, 34.9, and 49.4; and (c) *tbl* at $tU/\delta_0 = 0.0$, 21.1, 31.4, 37.5, and 61.4.

behavior of the maximum averaged dissipation with time. In the case of *HIGH1P*, the dissipation near the centerline increases throughout the computation, indicating that, in spite of the agreement cited above with the fully developed value, *HIGH1P* is probably out of equilibrium. The case *HIGH2P* is computed to considerably larger times, and the dissipation, after increasing slightly at first, then decreases, as would be expected for an equilibrium layer. In the case of *tbl* the dissipation grows rapidly from the initial condition, then decays similarly to *HIGH2P*.

Figure 5(a) shows the probability density function $F(-Q_S)$ and weighted probability density function $-Q_S F(-Q_S)$ over the entire volume of the mixing layer for the case *HIGH1P*. Most of the contribution to the

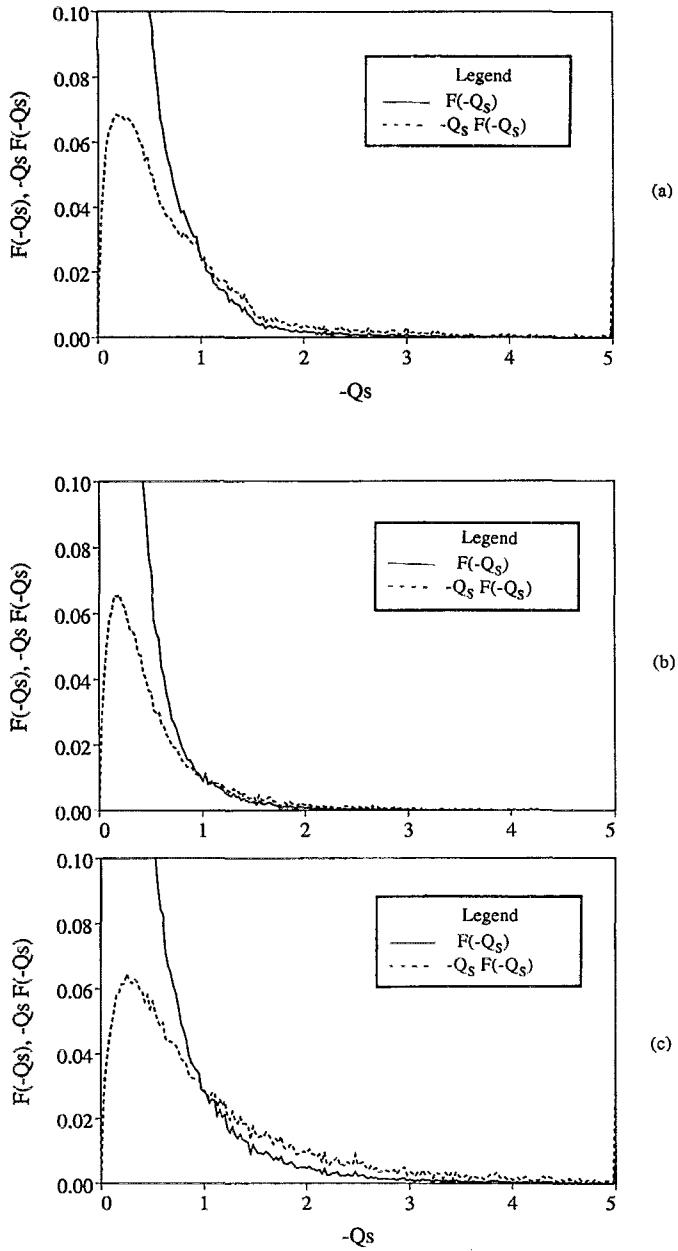

FIG. 5. Weighted probability density functions $F(-Q_S)$ and $(-Q_S)F(-Q_S)$ vs $-Q_S$ for (a) *HIGH1P* at $tU/\delta_0=25.3$, (b) *HIGH2P* at $tU/\delta_0=34.9$, and (c) *tbl* at $tU/\delta_0=37.5$.

volume-averaged $-Q_S$ comes from points with $-Q_S$ between 0 and 3. Although the far flung values of $-Q_S$ on the scatter diagram in Fig. 2(b) tend to follow interesting patterns, at the Reynolds number of this simulation, they contribute only a few percent of the total energy dissipation. This was one of the major reasons why it was felt that scatter diagrams should be replaced by number density or joint probability density diagrams with contours corresponding to the logarithm of the number density function, so that possible ridges could be seen in regions that are highly darkened in the scatter plots. Figures 5(b) and 5(c) show similar results for *HIGH2P* and *tbl*. The latter case shows a somewhat broader distribution than either of the two laminar initial condition cases.

Figure 6 shows a plot of the time history of the Reynolds number based on current vorticity thickness for the three cases of interest, and will be used later to define local length scales for making comparisons between *HIGH2P* and *tbl* at the same Reynolds number.

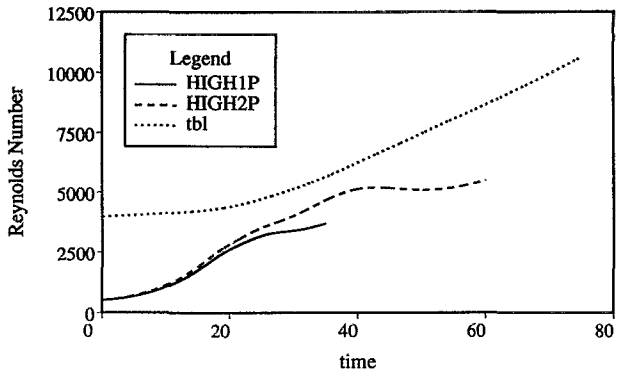

FIG. 6. Vorticity thickness Reynolds number R_δ vs nondimensional time for the incompressible mixing layers.

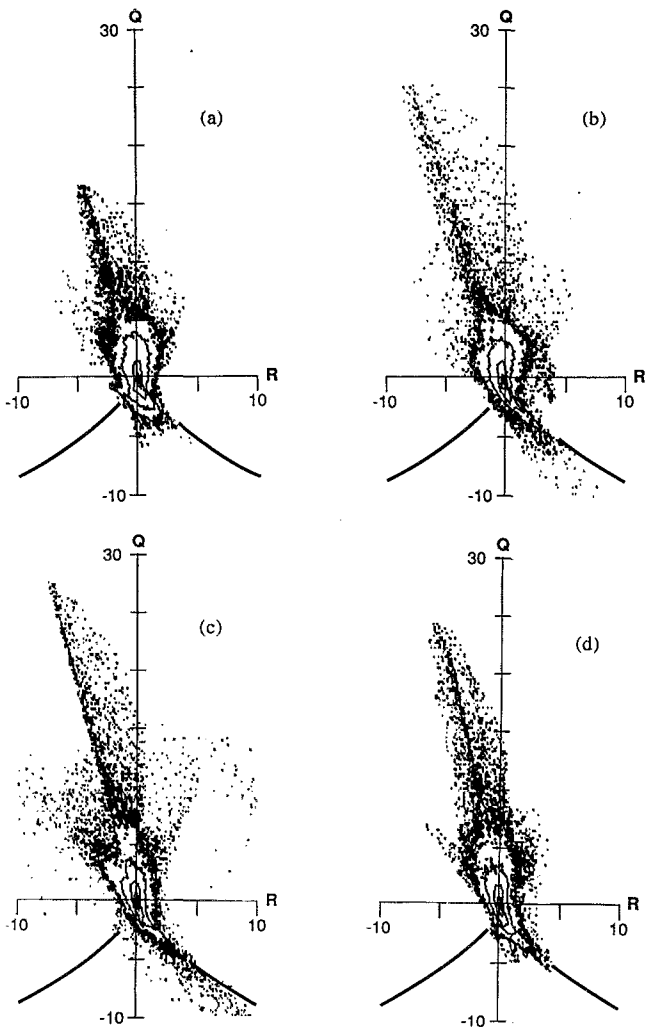

FIG. 7. Number density contour plot of Q vs R for *HIGH1P* at $tU/\delta_0=$(a) 19.3, (b) 22.3, (c) 25.3, and (d) 29.8.

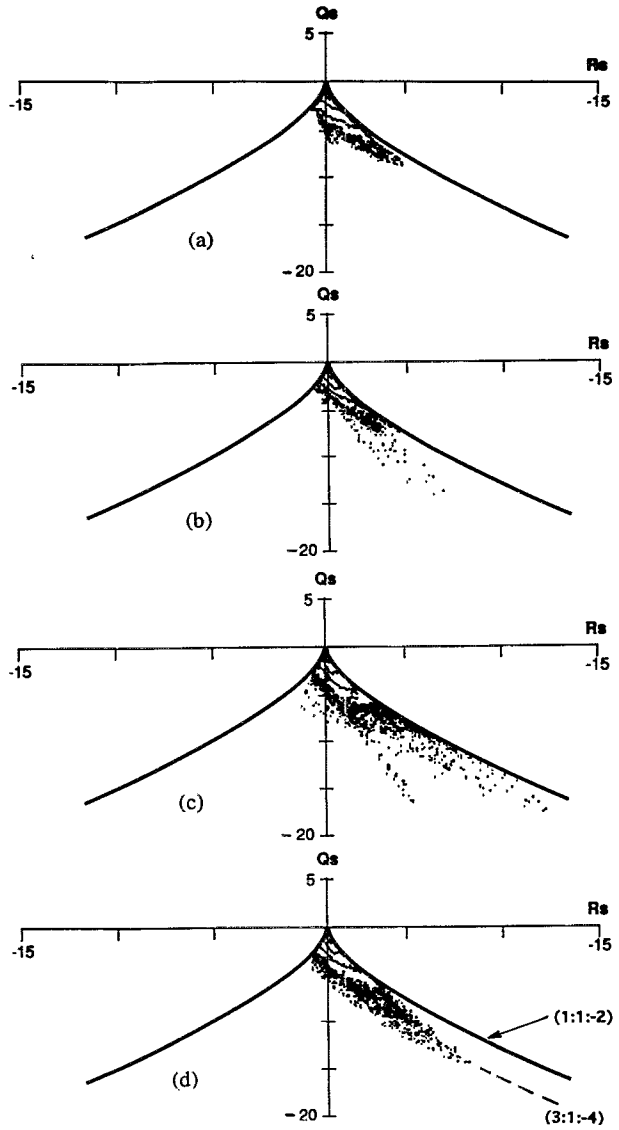

FIG. 8. Number density contour plot of Q_S vs R_S for *HIGH1P* at tU/δ_0=(a) 19.3, (b) 22.3, (c) 25.3, and (d) 29.8.

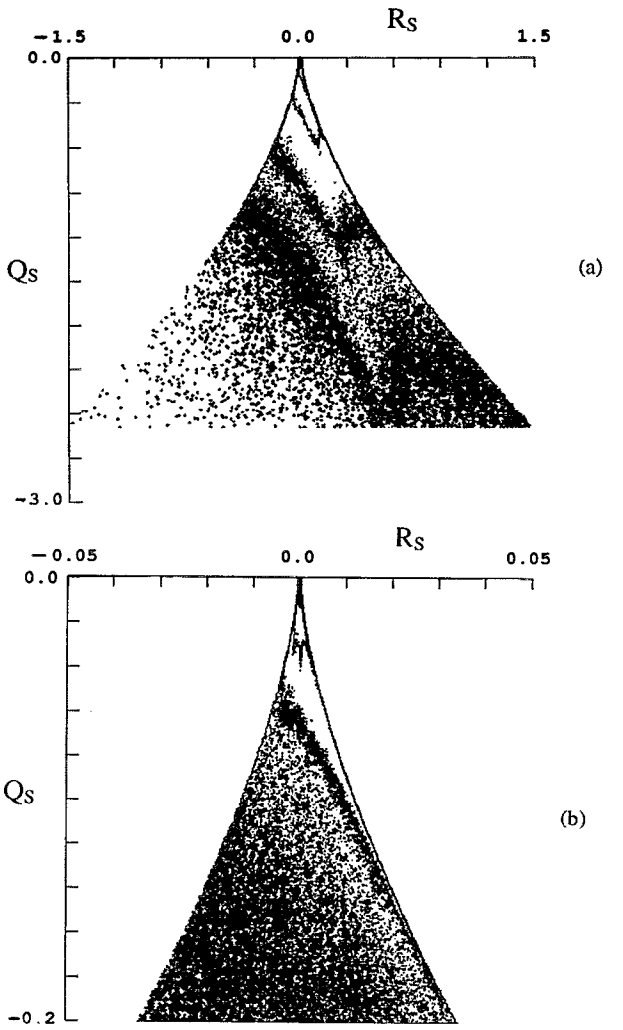

FIG. 9. Number density contour plot of Q_S vs R_S for *HIGH1P* at tU/δ_0=25.3. Axes magnified by a factor of (a) 10 and (b) 300.

D. Number density contour plots

Figures 7–10 show the number density contour plots for *HIGH1P*. Figures 11–14 show the results for *HIGH2P*, and Figs. 15–18 show the same for *tbl*. These results are similar to the scatter diagrams given in Fig. 2, but are corrected for nonuniform grid spacing and presented in the form of contour plots as discussed above.

1. The case HIGH1P

In the contour plots more structural features are apparent. A property of Figs. 7, 8, and 10 that is related to the previous discussion of Fig. 4(a) is that velocity gradients tend to increase with time. However, in contrast to the planar-averaged $-Q_S$ the points with the largest invariants show a slight decrease at the latest time depicted. In fully developed turbulent plane mixing layers, if dissipation scales with production, then according to Kolmogorov scaling, the velocity gradients should decrease with time. According to this reasoning, *HIGH1P* is underdeveloped with production exceeding dissipation for most, if not all, of the times shown. Perhaps the most striking feature of Fig. 7 is the very pronounced nearly straight ridge line extending into the upper left quadrant at all four times depicted (cf. Fig. 1; the topology stable-focus stretching). The points that form this ridge line are found in Fig. 10, extending along the horizontal axis, where they are found to be associated with extremely low rates of dissipation. Indeed, the most strongly rotational points in the flow are associated with nearly zero dissipation, suggesting that the flow is local in nearly solid body rotation. In physical space these points are found within the ribs that connect adjacent large spanwise rollers.[2] On the other hand, points with the highest dissipation in the flow tend to be associated with comparably strong enstrophy density, i.e., they lie along a roughly 45° line in Fig. 10 suggesting that the largest dissipation rates occur in sheets.

Figure 8 shows the evolution of the rate-of-strain invariants for *HIGH1P*. The most striking feature of these plots is the very pronounced preference for a rate-of-strain

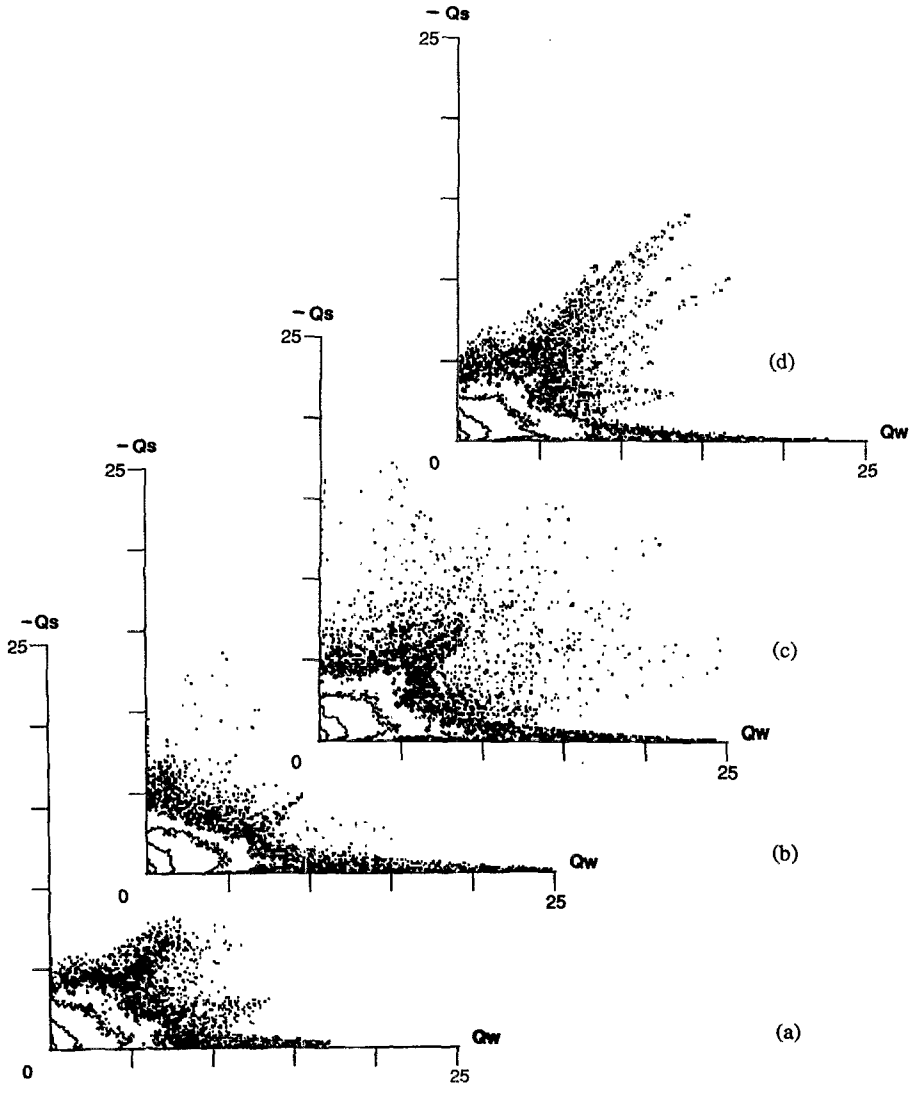

FIG. 10. Number density contour plot of $-Q_S$ vs Q_W for *HIGH1P* at $tU/\delta_0=$(a) 19.3, (b) 22.3, (c) 25.3, and (d) 29.8.

topology of the type saddle–saddle-unstable-node (two positive eigenvalues, one negative). Figure 9 shows the rate-of-strain invariants plotted at two magnifications to enable features near the origin to be viewed. These plots will be discussed further in Sec. VI.

2. The case HIGH2P

Figures 11–14 show the results for *HIGH2P*. The very largest gradients in this flow are quite different from the case *HIGH1P*, in spite of the similarities in the initial conditions. There is no pronounced ridge line in the upper left quadrant, but only a scattering of points, which constitute a very small fraction of the flow. These few points are found along the horizontal axis in Fig. 14, as might be expected. What is missing from Fig. 14 in comparison to Fig. 10 is the structure along a 45° line. Instead the dissipating points in *HIGH1P* appear to have a wide range of enstrophy density. Nevertheless, the strain invariants shown in Figs. 12 and 13 show the usual strong preference for positive R_S.

3. The case tbl

Figures 15–18 show the results for *tbl*, which started out as two turbulent boundary layers, and then developed to a much higher Reynolds number than *HIGH1P*. Figure 15 is most interesting. It shows that all data points for the turbulent boundary layer cluster near the origin of the Q vs R plot and suddenly explode to much larger values in the plane mixing layer. It should be noted that in the wall region of a turbulent boundary layer, Q and R are small, even though the gradients are not small, i.e., near the wall the two oppositely signed terms that make up the invariants are formed from the same quantities. Nevertheless, these pictures graphically illustrate how much larger velocity gradients become when the wall constraint of a turbulent boundary layer is removed. A clearer measure of the relative magnitudes of the velocity gradients can be inferred from Fig. 16, which involves only positive definite quantities, and indicates that indeed the gradients tend to grow substantially and then diminish at late times. The plots in Fig. 18 show that the turbulent boundary layer

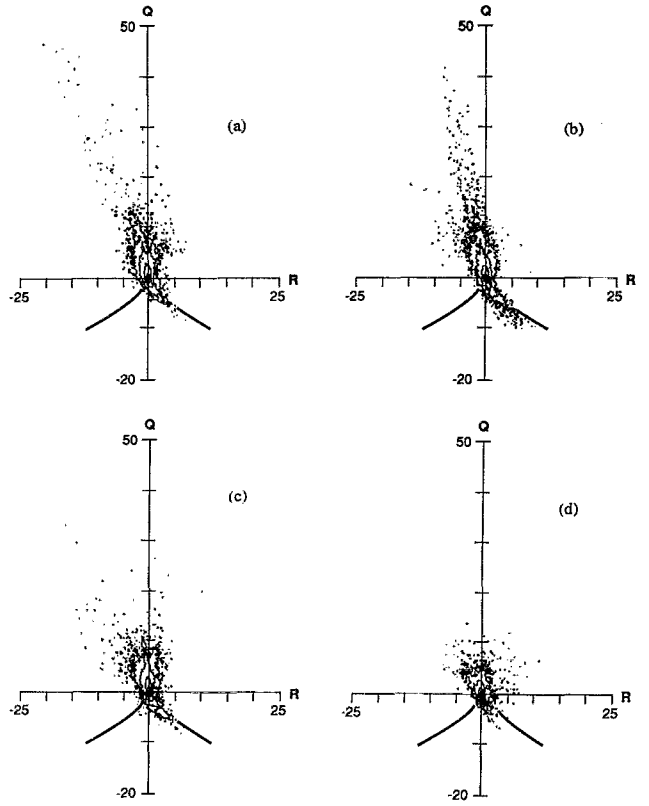

FIG. 11. Number density contour plot of Q vs R for *HIGH2P* at tU/δ_0=(a) 19.1, (b) 25.1, (c) 34.9, and (d) 49.4.

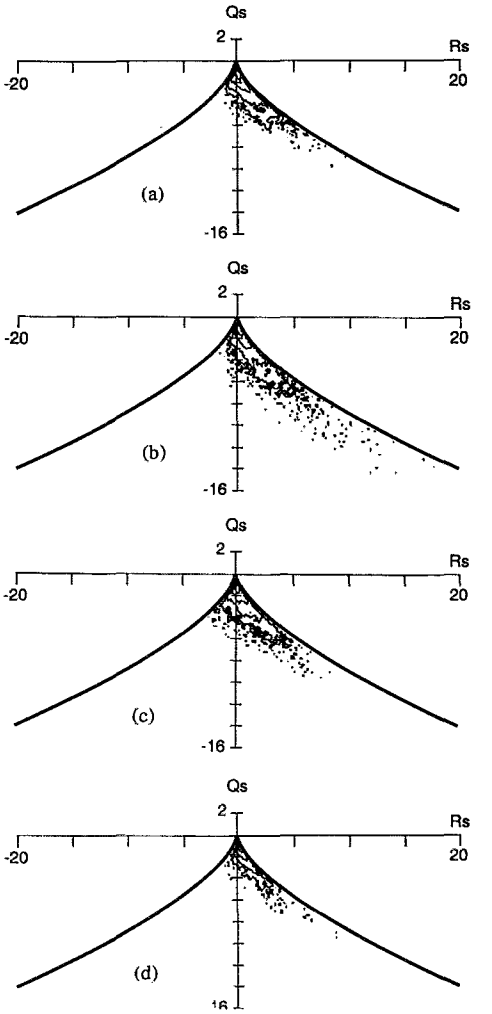

FIG. 12. Number density contour plot of Q_S vs R_S for *HIGH2P* at tU/δ_0=(a) 19.1, (b) 25.1, (c) 34.9, and (d) 49.4.

structures at $t'=0$ are sheet-like, but, in contrast to *HIGH1P*, there are no preferred structures revealed by the $-Q_S$ vs Q_W plot for later times, and there is no evidence whatsoever for a pronounced ridge line in the (Q,R) plane with strongly stable-focusing topology. As with *HIGH1P* and *HIGH2P*, the Q vs R plot shows that most points tend to cluster around the origin, with the main distribution of data lying in a roughly elliptical region with its major axis aligned with the upper left quadrant corresponding to the topology stable-focus-stretching and the lower right quadrant with the topology unstable node-saddle–saddle. The rate-of-strain invariants shown in Fig. 16 show the usual strong preference for $R_S>0$, consistent with the other cases. The very regular banded structure of the rate-of-strain invariants shown in Fig. 17 is quite interesting and will be discussed shortly.

The highly organized flow structures observed in *HIGH1P* and discussed in Chen *et al.*[2] are replaced by most complex structures in *tbl*. Vortex lines for *tbl* are shown in Figs. 19 and 20. Shown in Fig. 19 is the initial turbulent boundary layer and the attached eddies that lean approximately 45° to the mean flow direction are apparent. In Fig. 20 are shown vortex lines of the plane mixing layer after some development. Although no clear spanwise roll-ups are apparent from this vorticity plot, Fig. 21 shows instantaneous streamline patterns that close on themselves indicating a general spanwise roll-up at the largest scale of the flow.

V. MODELS OF THE EVOLUTION OF THE VELOCITY GRADIENT TENSOR

Figures 7, 11, and 15 show a series of snapshots of the current values of Q and R for a large number of fluid elements at various stages in the evolution of the flow. There are three salient features of these plots.

(1) A significant fraction of the data lies in the lower right quadrant along the $(R>0,\ D=0)$ branch. These points tend to be characterized by relatively high rates of kinetic energy dissipation.

(2) By far the preponderance of points collects in a roughly elliptical region about the origin, with its major axis aligned with the upper left and lower right quadrants.

(3) For certain cases, a small fraction of the data extends a considerable distance into the upper left quadrant. For points far from the origin, the local vorticity strongly dominates the local strain. Moreover, points far from the origin tend to be associated with relatively small rates of kinetic energy dissipation (cf. Figs. 10, 14, and 18). Such points are quite common in *HIGH1P*, less so in *HIGH2P*, and extremely rare in *tbl*. The presence or absence of these

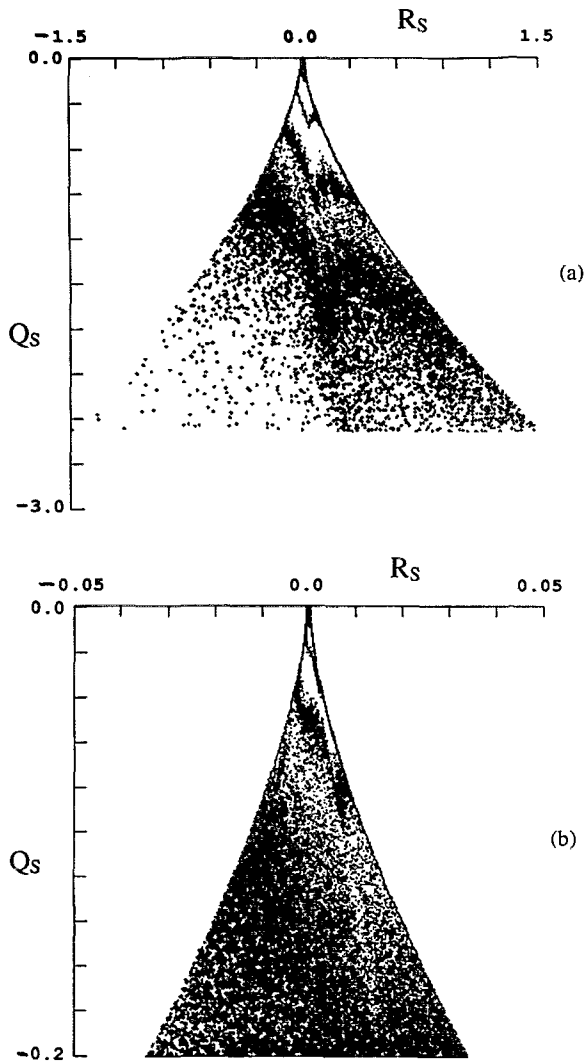

FIG. 13. Number density contour plot of Q_S vs R_S for *HIGH2P* at $tU/\delta_0=34.9$. Axes magnified by a factor of (a) 10 and (b) 300.

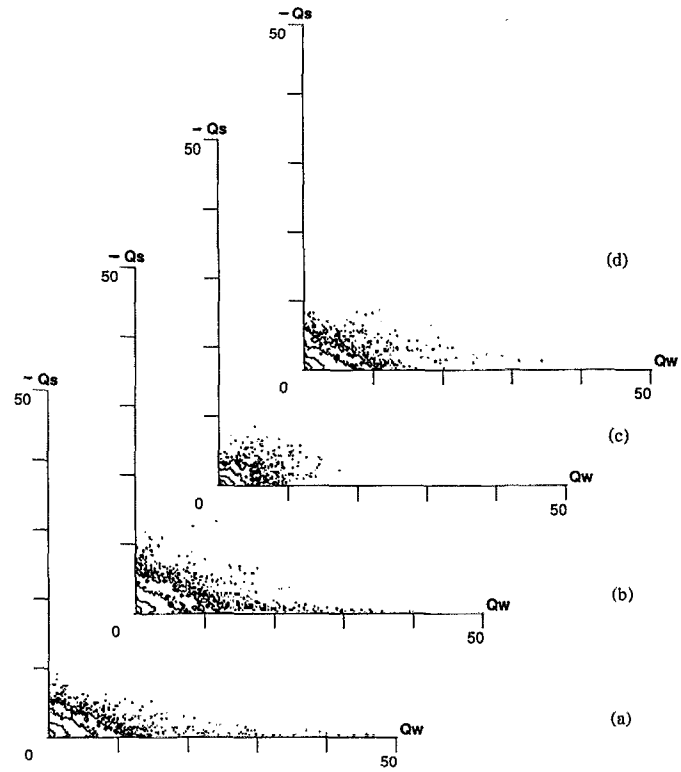

FIG. 14. Number density contour plot of $-Q_S$ vs Q_W for *HIGH2P* at $tU/\delta_0=$(a) 19.1, (b) 25.1, (c) 34.9, and (d) 49.4.

kinds of motions appears to be closely related to the regularity of the initial conditions. These features of the Q–R plots have been observed in a variety of inhomogeneous flows,[10] suggesting that they may be universal. While the Q-R plots are not yet fully understood, transport equations for A_{ij}, Q, and R can be generated from the equations of motion and studied. These studies do give some insight into the shapes of the invariant plots. Analysis of solutions of a restricted Euler model for the evolution of A_{ij},[11] together with a fairly general analysis of the equations for Q and R, suggests that the velocity gradient tensor in three-dimensional flow tends to evolve toward an attractor in the space of tensor invariants.[12] In addition, these studies suggest that in a general flow the rate-of-strain and rate-of-rotation tensors should evolve to a configuration with two positive principal rates of strain and the vorticity aligned with the smaller positive strain. The shape of the attracting region closely resembles the distribution of points seen in Figs. 7, 11, and 15 (see Fig. 4 in Ref. 12).

VI. THE GEOMETRY OF DISSIPATION

From (11) and (12), it can be seen that Q_S normalized by the current vorticity thickness scales with R_δ, and, therefore, it seems likely that R_S should scale with $R_\delta^{3/2}$. This would imply that the data should follow a curve,

$$|R_S| \propto (|Q_S|)^{3/2}. \tag{13}$$

This relationship is what one might expect purely on dimensional grounds, but there is no rigorous proof. It is interesting to note that such a curve on the Q_S vs R_S plot represents a rate of strain geometry, where the principal rates of strain α, β, and γ are in a constant ratio to one another. For the data set *HIGH1P*, points of high dissipation follow closely the curve corresponding to the ratio of $\alpha{:}\beta{:}\gamma=3{:}1{:}-4$ [see Fig. 8(d)], which was observed by Ashurst *et al.*[9] in studies of forced isotropic turbulence. In addition, as noted by Sondergaard *et al.*,[10] who studied a variety of inhomogeneous shear flows, the vorticity vector tends to align itself with the second principal rate of strain β. It should be noted that while other data sets analyzed by Sondergaard *et al.*[10] show the same vorticity alignment, the $3{:}1{:}-4$ ratio of rates of strain is not always observed. The Q_S vs R_S plots for *tbl* shown in Fig. 16, indicate that the strain rates in this case tend to follow a different curve, closer to the real–imaginary dividing surface (6) corresponding to $\alpha{:}\beta{:}\gamma=1{:}1{:}-2$. Hence, this aspect of the fine-scale motion appears to be dependent on initial conditions and is also very likely dependent on Reynolds number. The

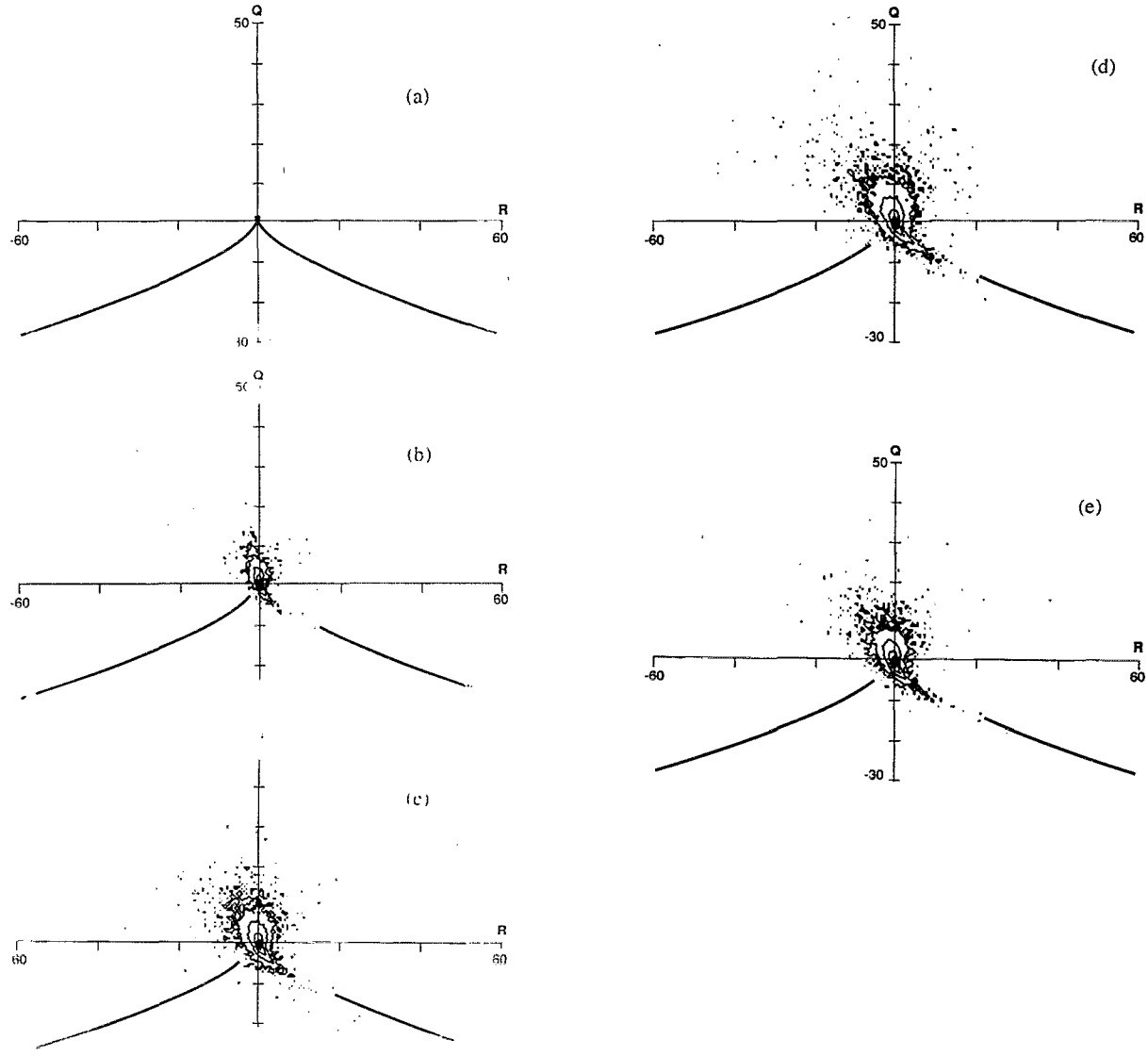

FIG. 15. Number density contour plot of Q vs R for *tbl* at $tU/\delta_0=$(a) 0.0, (b) 21.1, (c) 31.4, (d) 37.5, and (e) 61.4.

dependence on Reynolds number is apparent from the variation with time of the Q_S vs R_S plots for a given flow.

The results depicted in Figs. 8, 12, and 16 show that motions characterized by high rates of dissipation (large $-Q_S$) clearly show a preference for $R_S>0$, corresponding to a local topology of the rate of rate-of-strain tensor that is of the type saddle–saddle-unstable node (cf. Fig. 1). It appears that, with a modest amount of scatter, the fine-scale motions with the largest gradients follow a relationship of the form

$$R_S \cong K(-Q_S)^{3/2}. \tag{14}$$

The positive quantity K is expected to be a function of Reynolds number and initial conditions with an upper limit of $K=2\sqrt{3}/9$ corresponding to locally axisymmetric flow ($\alpha:\beta:\gamma=1:1:-2$). The relation (14) appears to characterize the highest dissipating points in the flow. However, as was pointed out earlier, these points constitute only a small fraction of the total dissipation. It is therefore of interest to investigate the dissipation associated with intermediate and large scales, particularly with values in the range $0<-Q_S<3$, which, as was pointed out earlier, contribute the bulk of the dissipation.

This brings us to the discussion of Figs. 9, 13, and 17; the magnified plots of the rate-of-strain invariants. Figures 9(a), 13(a), and 17(a) show the number density contours plotted over the range of Q_S, which contributes the bulk of the total dissipation. Figures 9(b), 13(b), and 17(b) show a range of Q_S that encompasses the largest scales in the flow. Note that throughout this paper we have used the initial thickness, δ_0, for normalizing velocity gradients. This leads to typical values of Q_S on the order of 0.01–0.02 for large eddies that span the flow. The most striking feature of all three plots is that the rate-of-strain tensor strongly prefers the topology unstable-node-saddle–saddle at intermediate and large scales (Q_S close to zero). This

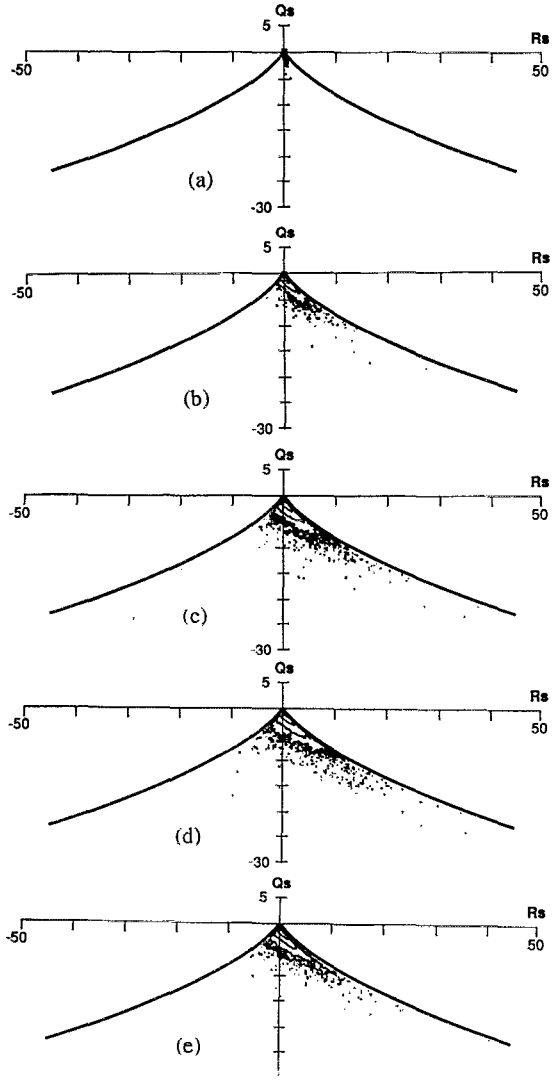

FIG. 16. Number density contour plot of Q_S vs R_S for *tbl* at $tU/\delta_0=$(a) 0.0, (b) 21.1, (c) 31.4, (d) 37.5, and (e) 61.4.

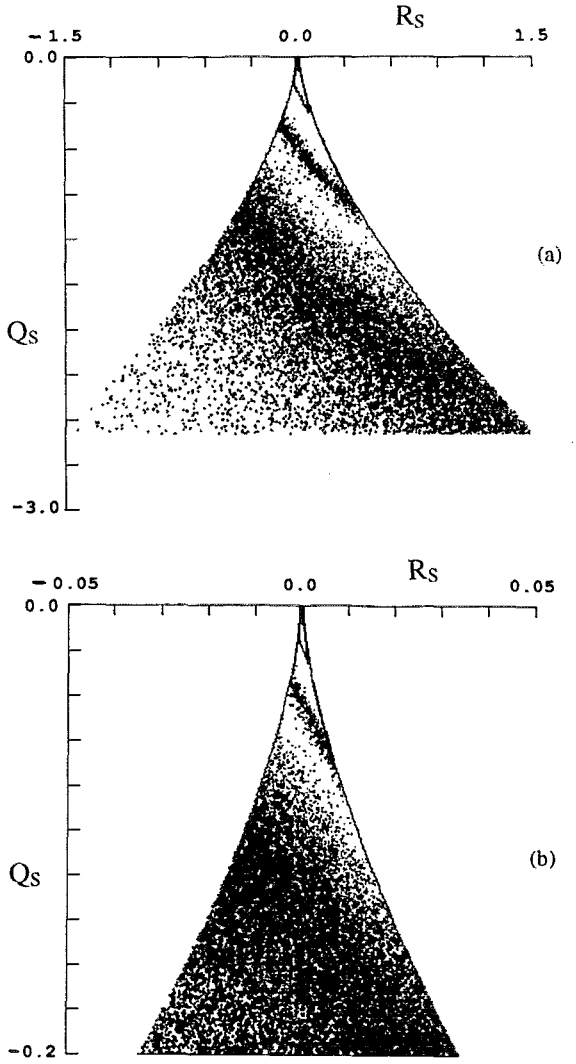

FIG. 17. Number density contour plot of Q_S vs R_S for *tbl* at $tU/\delta_0=37.5$. Axes magnified by a factor of (a) 10 and (b) 300.

rate-of-strain geometry is not just a property of the fine scales. Another interesting feature is that structures that mark the finest scales can sometimes be traced well into the region of intermediate scales. The ridge line penetrating into the lower right portion of Fig. 9(a) (case *HIGH1P*) is the continuation of the same structure that can be seen approximately midway across the right side of Fig. 8(c). A similar ridge line can be seen in Fig. 13(a) (case *HIGH2P*), although its continuation in Fig. 12(c) is not so apparent.

Before discussing these plots further we need to make a brief digression. It has been pointed out by Jimenez[13] that, in the neighborhood of a localized region of stretched vorticity, when the maximum vorticity is much larger than the ambient, the velocity gradient tensor will tend to be of the form

$$A_{ij}=\begin{bmatrix} A_{11} & A_{12} & 0 \\ A_{21} & A_{22} & 0 \\ 0 & 0 & b \end{bmatrix}, \tag{15}$$

where the out of plane rate of strain, b, is positive. It should be pointed out that the velocity gradient tensor at any point in the flow can be put in the form (15) by use of an affine transformation.[1] In the event that the real eigenvalue, b, is constant over a finite volume of the flow then such a region can be regarded as a locally two-dimensional flow with out of plane strain. An axisymmetric example of such a flow is the Burger's vortex. For such a flow, at the radius of maximum dissipation surrounding the vorticity maximum, the rate-of-strain tensor will tend to have two positive eigenvalues and the vorticity will tend to be aligned with the smaller positive principal rate-of-strain direction. It can be easily shown that the invariants of (15) satisfy

$$R+bQ+b^3=0. \tag{16}$$

In Ref. 12 a basic analysis of the equations of motion is used to show that flow structures characterized by (16) should evolve as typical features of turbulent flow. For any value of b there exists a point of oscillation between (16)

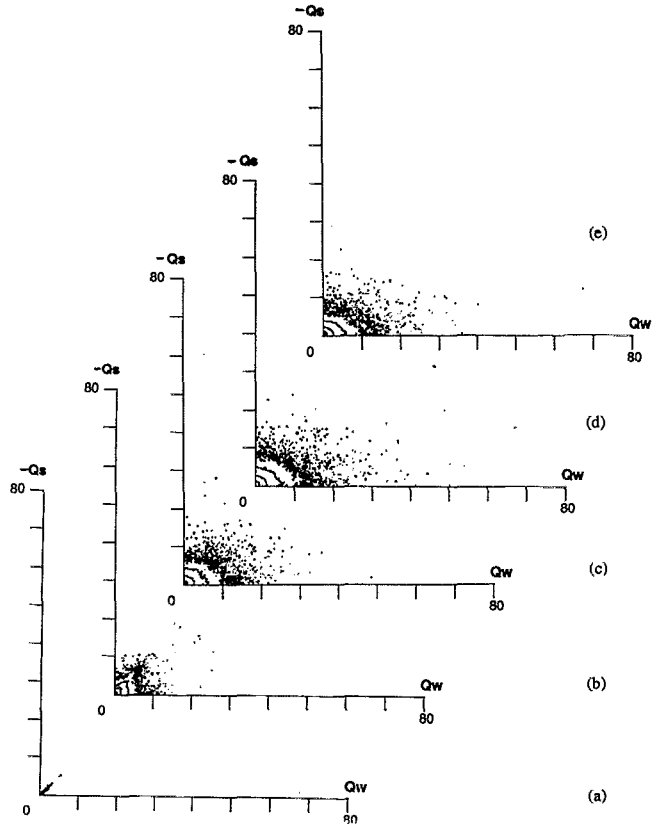

FIG. 18. Number density contour plot of $-Q_S$ vs Q_W for *tbl* at tU/δ_0=(a) 0.0, (b) 21.1, (c) 31.4, (d) 37.5, and (e) 61.4.

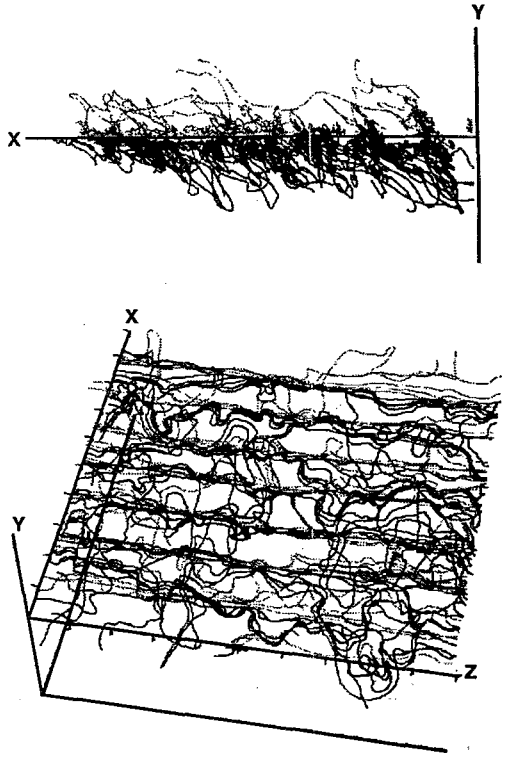

FIG. 19. Vortex lines for *tbl* at tU/δ_0=0.0.

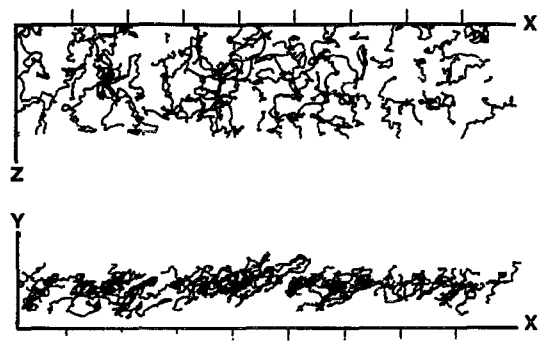

FIG. 20. Vortex lines for *tbl* at tU/δ_0=76.3.

and (6); thus, for $-\infty < b < \infty$, the straight line (16) is the generator of (6). It can be easily shown that the rate-of-strain invariants of (15) satisfy

$$R_S + bQ_S + b^3 = 0. \tag{17}$$

Based on this simple kinematical arguement and the relatively straight banded structure of the number density contours seen in these figures, particularly Figs. 9(b) and 17, it would appear that the dominant topological structure of the intermediate scales that are responsible for the bulk of the dissipation is that of a locally two-dimensional flow with out-of-plane straining. The number density contours in Fig. 17 for the case *tbl* are particularly interesting. Although there is some curvature evident in the contours, the straight line relationship (17) approximately describes the behavior of the invariants throughout the range of intermediate scales and up into the range of large scales. For the *tbl* flow, the joint PDF of rate-of-strain tensor invariants appears to be self-similar at intermediate and large scales.

In general, the rate-of-strain invariant data suggests that the relationship (14) describes the strongest dissipating motions at the finest scales, while the relationship (17) seems to hold for intermediate scale motions that accomplish most of the dissipation.

VII. COMPARISON OF LAMINAR AND TURBULENT INITIAL CONDITIONS AT THE SAME REYNOLDS NUMBER

From Fig. 6, it can be seen that there is an overlap of Reynolds numbers for *HIGH2P* and *tbl*. In fact, they both share a Reynolds number of 5000, as indicated in the figure. Figures 22(a) and 22(b) show Q vs R plots of *tbl* and *HIGH2P*, each scaled with the current vorticity thickness and appropriate velocity U. The vorticity thickness in each case has grown considerably, and this accounts for the

FIG. 21. Streamlines for *tbl* at tU/δ_0=76.3.

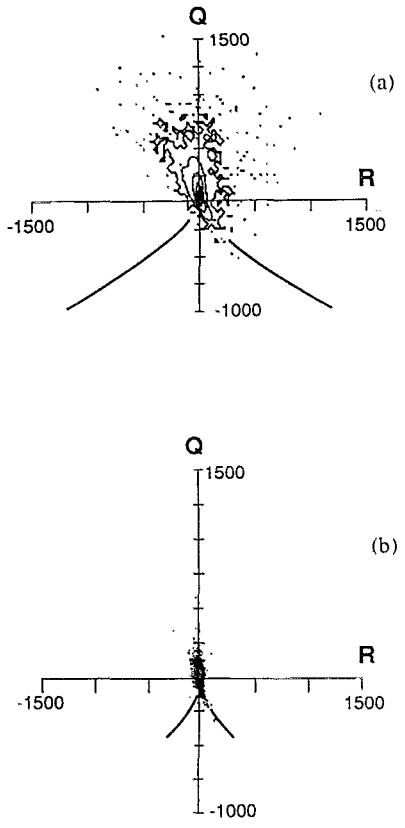

FIG. 22. Rescaled number density contour plot of Q vs R for (a) *HIGH2P* at $tU/\delta_0=49.4$ and (b) *tbl* at $tU/\delta_0=61.4$.

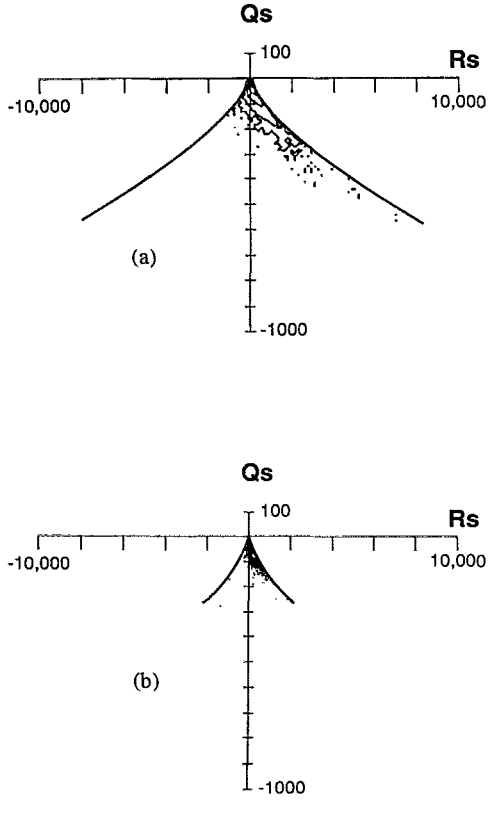

FIG. 23. Rescaled number density contour plot of Q_S vs R_S for (a) *HIGH2P* at $tU/\delta_0=49.4$ and (b) *tbl* at $tU/\delta_0=61.4$.

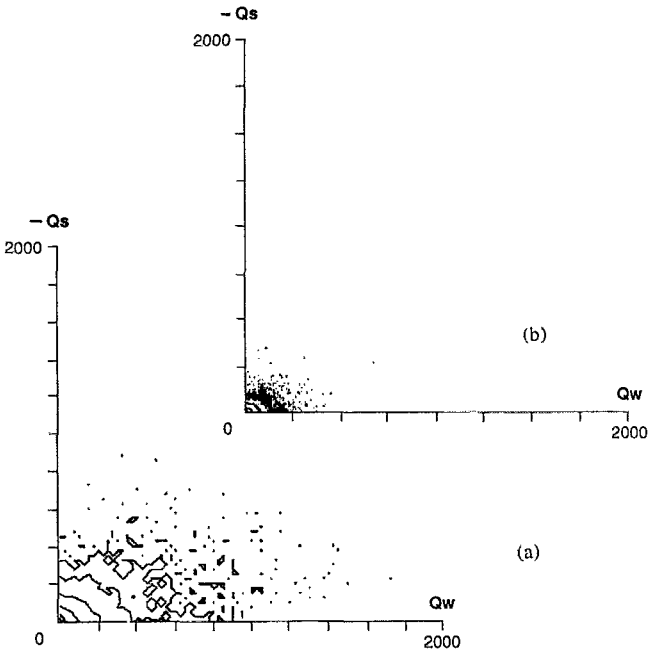

FIG. 24. Rescaled number density contour plot of $-Q_S$ vs Q_W plots for (a) *HIGH2P* at $tU/\delta_0=49.4$ and (b) *tbl* at $tU/\delta_0=61.4$.

much larger numbers on the axes in the plots of rescaled invariants in Figs. 22–24. Figures 23 and 24 show the corresponding Q_S vs R_S and $-Q_S$ vs Q_W plots for comparison. Although the shapes of the plots are roughly the same, there appears to be a major difference in the scaling, indicating that the velocity gradients normalized by the current thickness in *tbl* are considerably lower than in *HIGH2P* for the same Reynolds number. This is consistent with the lower growth rate of *tbl* compared to *HIGH2P* seen in Figs. 4(b) and 4(c); by the time *tbl* has reached the same thickness as *HIGH2P* the normalized gradients in *tbl* have dropped considerably in comparison.

VIII. CONCLUSIONS

In all flow cases considered here, motions over the bulk of the flow volume were distributed in a roughly elliptical region about $(Q,R)=(0,0)$, with the major axis aligned with the upper left and lower right quadrants. In the case designated as *HIGH1P*, the flow is initiated from a laminar layer with an error function profile, and the maximum Reynolds number R_δ to which the flow evolves is approximately 3000. Here, the highly dissipative motions are always accompanied by high enstrophy, indicating a vortex sheet-like structure, although the highest enstrophy motions are situated in tube-like structures in nearly solid body rotation. In the case *HIGH2P*, the tube-like structures are much less apparent.

The rate-of-stain tensor in all three cases indicated that dissipating points were of the topology unstable-node-saddle–saddle ($R_S>0$), with the largest rates of strain tending toward a fixed ratio. Examination of magnified (Q_S,R_S) plots indicated that the tendency toward $R_S>0$ characterizes the full range of motions responsible for vir-

tually all the dissipation. At intermediate scales the rate-of-strain invariants tend to approximately follow a straight line relationship characteristic of a two-dimensional flow with out-of-plane straining.

In the case of *tbl*, which was initiated from two turbulent boundary layers placed back to back, the highest local Reynolds number considered was $R_\delta = 9000$. Here, the $-Q_S$ vs Q_W plots indicated no pronounced tube-like structures, as in the cases initiated with laminar initial conditions. The Q–R plots did indicate a general preference for stable-focus stretching and the Q_S vs R_S plots showed that the highly dissipating motions tend to $\alpha{:}\beta{:}\gamma = 1{:}1{:}-2$. In this case the intermediate-scale motions showed the clearest tendency for Q_S and R_S to follow a straight line.

Comparison was made of two flows at the same Reynolds number, but with laminar and turbulent initial conditions. Care was taken to normalize the data with the local layer thickness. Although the shape of the invariant plots are roughly the same, there appears to be a major difference in the scaling, indicating that the velocity gradients in *tbl* are considerably smaller than in *HIGH2P* for the same Reynolds number.

ACKNOWLEDGMENTS

We would like to acknowledge the invaluable assistance of Dr. Michael Rogers and Dr. Robert Moser of the NASA–Ames Research Center in obtaining and understanding the data sets upon which this study is based. We would also like to acknowledge support from ONR Grant No. N00014-90-J-1976, the Center of Turbulence Research, and C.S.I.R.O. Finally, this paper is dedicated to Bill Reynolds on the occasion of his 60th birthday and in recognition of his intellectual leadership that has influenced and inspired generations of turbulence researchers at Stanford and throughout the world.

[1]M. S. Chong, A. E. Perry, and B. J. Cantwell, "A general classification of three-dimensional flow fields." Phys. Fluids A **2**, 765 (1990).
[2]J. H. Chen, M. S. Chong, J. Soria, R. Sondergaard, A. E. Perry, M. Rogers, R. Moser, and B. J. Cantwell, "A study of the topology of dissipating motions in direct numerical simulations of time-developing compressible and incompressible mixing layers," Proceedings of the Center for Turbulence Research Summer Program, CTR-S90, 1990.
[3]J. M. Lopez and C. J. Bulbeck, "Behavior of streamwise rib vortices in a three-dimensional mixing layer" Phys. Fluids A **5**, 1694 (1993).
[4]R. Moser and M. Rogers, "Mixing transition and the cascade to small scales in a plane mixing layer," IUTAM Symposium on Stirring and Mixing, La Jolla, CA, 20–24 August 1990.
[5]R. Moser and M. Rogers, "The three-dimensional evolution of a plane mixing layer: Pairing and transition to turbulence," J. Fluid Mech. **247**, 275 (1993).
[6]P. R. Spalart, "Direct simulation of a turbulent boundary layer up to $R_\theta = 1410$," J. Fluid Mech. **187**, 61 (1988).
[7]J. Chen, "The effect of compressibility on conserved scalar entrainment in a plane free shear layer," 8th Symposium on Turbulent Shear Flows, Munich, 1991.
[8]P. B. Bradshaw and D. H. Ferriss, "The spectral energy balance in a turbulent mixing layer," Aeronautical Research Council Current Paper No. 899, 1967.
[9]W. T. Ashurst, A. R. Kerstein, R. M. Kerr, and C. H. Gibson, "Alignment of vorticity and scalar gradients with strain rate in simulated Navier–Stokes turbulence," Phys. Fluids **30**, 2343 (1987).
[10]R. Sondergaard, J. Chen, J. Soria, and B. J. Cantwell, "Local topology of small scale motions in turbulent shear flows," in Ref. 7.
[11]B. J. Cantwell, "Exact solution of a restricted Euler equation for the velocity gradient tensor," Phys. Fluids A **4**, 782 (1992).
[12]B. J. Cantwell, "On the behavior of velocity gradient tensor invariants in direct numerical simulations of turbulence," Phys. Fluids A **5**, 2008 (1993).
[13]J. Jimenez, "Kinematic alignment effects in turbulent flows," Phys. Fluids A **4**, 652 (1992).